# From poison to promoter: investigation of supported rhodium sulphides as heterogeneous hydroformylation catalysts

Arjun Neyyathala[1], Edvin Fako[2], Sandip De[2], Daria Gashnikova[3], Florian Maurer[3], Jan-Dierk Grunwaldt[3,4], Stephan A. Schunk[2,5,6] and Schirin Hanf[1*]

[1]Institute for Inorganic Chemistry, Karlsruhe Institute of Technology, Engesserstr. 15, 76131 Karlsruhe, Germany.

[2]BASF SE, Carl-Bosch Str. 38, 67056 Ludwigshafen, Germany.

[3]Institute for Chemical Technology and Polymer Chemistry, Karlsruhe Institute of Technology, Engesserstr. 18 / 20, 76131 Karlsruhe, Germany.

[4]Institute of Catalysis Research and Technology (IKFT), Hermann-von-Helmholtz-Platz 1, 76344 Eggenstein-Leopoldshafen, Germany

[5]hte GmbH, the high throughput experimentation company, Kurpfalzring 104, 69123 Heidelberg, Germany.

[6]Institute of Chemical Technology, Faculty of Chemistry and Mineralogy, Leipzig University, Linnéstr. 3, 04103 Leipzig, Germany.

## Abstract

Herein we report the use of supported nanoparticles of crystalline rhodium sulphides as active heterogeneous catalysts for the hydroformylation of alkenes showing an excellent selectivity towards the aldehyde products. It was found that supported $Rh_xS_y$ (x=17, y=15 or x=2, y=3 with 1 and 10 wt.% Rh) nanoparticles greatly outperform pure Rh nanoparticles in terms of activity, with $Rh_{17}S_{15}/SiO_2$ being the superior catalyst candidate. The TOF for the hydroformylation of styrene, determined for the lead system $Rh_{17}S_{15}/SiO_2$ (1 wt.% Rh), is with 2620 $h^{-1}$ significantly higher than TOF values reported for rhodium phosphide-based systems. As the presence of S in the Rh sulphides introduces structural diversity in the bulk as well as the range of potential catalytic surfaces, we enumerate all possible terminations, use local environment descriptors combined with unsupervised Machine learning techniques and DFT to draw structure performance relationships. We find that the presence of S on the surface and in close proximity to the catalytic site had a profound impact on the chemical behavior of the catalyst, thus unlocking the tunability of the surface catalytic properties. This allows for the affinity towards the substrate to be modulated to a high degree ranging from S rich Rh-top like sites of low; to Rh rich, and in particular for $Rh_{17}S_{15}$, ($Rh_4$) sites with adsorption energies rivaling those of pristine Rh and improved spatial resolution.

## Introduction

The hydroformylation of alkenes using syn gas for the synthesis of aldehydes is one of the very important chemical transformations on industrial level, with an annual global aldehyde manufacturing exceeding 24 million metric tons year[1–5]. The relevance of aldehydes is based on their application as intermediates for the synthesis of alcohols, carboxylic acids, esters and amines, among others, which are essential for the production of pharmaceuticals, agrochemicals and other fine chemical products[2,6]. Up to know homogeneous rhodium-based catalysts are the preferred catalyst technology in the area of hydroformylation catalysts, as rhodium has proven to be the most active metal and the selectivity can in general be tuned via the ligand or the reaction conditions[7–11]. However, the use of a homogeneous catalyst involves technical challenges in the catalyst separation and recycling and the loss of precious metal must be avoided[12,13]. Consequently, heterogenized or heterogeneous rhodium catalysts as alternative candidates for oxo-chemistry, such as anchored Rh complexes on solid supports[14–16] and rhodium-containing nanoparticles[13,17] have gained significant research interest in the last decade.

A number of approaches in the field of heterogeneous catalysis pursue the mimicking of the steric and electronic environment of an active metal in homogeneous catalysts through the combination of a noble metal together with another less noble metal or non-metal to form alloys[17–22], intermetallic compounds[13] or other main-group containing metal phases[23,24]. In this context, also Rh-based systems, such as Rh-Zn[13], Rh-Co[19,25], and Rh-P[17] have been described applied as catalysts useful for hydroformylation reactions. The superior catalytic performance compared to pure metallic rhodium-based catalyst, in liquid[21] and gas phase hydroformylations[17] was already reported for supported rhodium phosphides, $Rh_2P$. Their catalytic activity was attributed to the formation of undercoordinated Rh species on the surface of the crystalline nanoparticles, a motif that can be compared to frustrated single sites in homogeneous catalysis[14,17]. Not only the inherent structural features of $Rh_2P$ contribute to its excellent catalytic activity, but also the electronic state of rhodium is modulated via a shift of the d-band center towards lower energy level relative to fermi level in comparison to pure Rh. This apparently leads to an optimal CO binding strength resulting in superior reactivity[21]. The generation of specific structural motifs has also been investigated in the case of the incorporation of Co into Rh and the synthesis of supported $RhCo_3$, where Rh-Co hybrid sites and $Rh_3$ ensembles were witnessed. Through these structural motifs and the therewith involved Co induced strain and ensemble effects, the binding energies of CO and propanal are carefully tailored, leading to a high selectivity towards C3 oxygenates in the vapor-phase hydroformylation of ethylene[19].

Herein we demonstrate a case, more precisely supported nanoparticles of crystalline rhodium sulphides, where the guiding principle is taken beyond emulating the parent metal's activity with a p-loaded surrogate, resulting in substantially improvements of the activity and selectivity in the hydroformylation of alkenes. Despite the fact, that sulphur is considered to be a typical catalyst poison or strong moderator for transition metals in catalysis, only recently metal sulphide phases, such as palladium sulphides have been explored as catalysts for the semi hydrogenation of

alkynes[26] and in the framework of electro catalysis[27–29]. With this work we now explore the use of supported rhodium sulphide nanoparticles, with a particular focus on the metal rich $Rh_{17}S_{15}$ and metal lean $Rh_2S_3$ phases, towards the use in liquid phase hydroformylation reactions of alkenes. Hereby the order of activity was determined as $Rh_{17}S_{15}$>$Rh_2S_3$>Rh, showing that the incorporation of sulphur into rhodium leads to a boost in catalytic activity, which is undermined by experimental and theoretical findings. We herein illustrate experimental and theoretical proof of the active sites in the form of $Rh_4$ hollow sites relevant for the $Rh_{17}S_{15}$ catalyst. The supported rhodium sulphide catalysts were recovered after the catalytic reactions and reused multiple times without the loss of catalytic activity, exhibiting great stability.

**Synthesis and characterization of supported rhodium sulphide particles**

The two rhodium sulphide phases selected for this investigation are the metal rich $Rh_{17}S_{15}$ (Rh/S = 1.13) and the metal lean $Rh_2S_3$ (Rh/S = 0.66) phase. For both phases a substantial performance difference can be expected due to the variation in Rh to S ratio. The silica supported rhodium sulphides particles were synthesized using an incipient wetness impregnation method of reactive precursors. Rhodium acetate ($Rh(OAc)_3$) and thiourea ($CH_4N_2S$) were dissolved in water and added dropwise to silica. The impregnated precursors were subsequently dried and brought to reaction via a thermal treatment in a flowing stream of argon to obtain the supported $Rh_xS_y$ phases. Since a loss of sulphur is occurring during the thermal treatment, the addition of an excess quantity of sulphur precursor (in this case thiourea) is required to compensate the loss and enable the $Rh_xS_y$ phase formation[30]. Hence, 20 mol%, 30 mol% and 50 mol% excess of thiourea with respect to the stoichiometric ratio of the corresponding sulphide, were impregnated on silica with $Rh(OAc)_3$ and the resulting product was heated in a flowing stream of argon at 700°C in order to synthesis the supported $Rh_{17}S_{15}$ material (10 wt.% Rh). Whereas an excess of 20 mol% and 50 mol% of thiourea resulted in the formation of metallic Rh nanoparticles and nanoparticles of the $Rh_{17}S_{15}$ phase, respectively, 30 mol% excess led to the formation of the phase pure $Rh_{17}S_{15}/SiO_2$ nanoparticles on silica (Figure 1a and S1). A further increase of the temperature to 750°C with the aim to enhance both the crystallinity and the crystallite size of the supported sulphides materials, thereby obtaining improved powder X ray diffraction reflexes, only resulted in the loss of sulphur and in the consequent formation of metallic nanoparticles of Rh well visible through X-ray diffraction (Figure S2). Different flow rates of argon were applied for the thermal treatment to study the influence on the phase formation. A flow rate of 15 Nl/h argon for the synthesis of $Rh_{17}S_{15}/SiO_2$ (10 wt.% Rh) resulted in the formation of mixed phases consisting of $Rh_{17}S_{15}$ and $Rh_2S_3$, whereas an increased flow rate of 450 Nl/h leads to the formation of phase pure $Rh_{17}S_{15}$ (Figure 1b). A higher argon flow rate can increase the transfer of volatile sulphur species via the gas phase and remove the excess S from material. Similarly, $Rh_2S_3/SiO_2$ (10 wt.% Rh) was synthesized via incipient wetness impregnation and a subsequent thermal treatment in a flowing stream of Ar (450 Nl/h) at 700°C with 50% excess thiourea to ensure the phase formation (Figure 1a). Catalyst materials, as described above, were also prepared with a lower absolute metal loading (1 wt.% Rh) to allow for a reduced size of the nanoparticles through limited sintering processes[31]. In addition,

inductively coupled plasma atomic emission spectrometry (ICP-AES) analyses were performed to determine the exact rhodium content of 1.03 wt.% in $Rh_{17}S_{15}/SiO_2$ (1 wt.% Rh) and 0.88 wt.% in $Rh_2S_3/SiO_2$ (1 wt.% Rh) (Table S9).

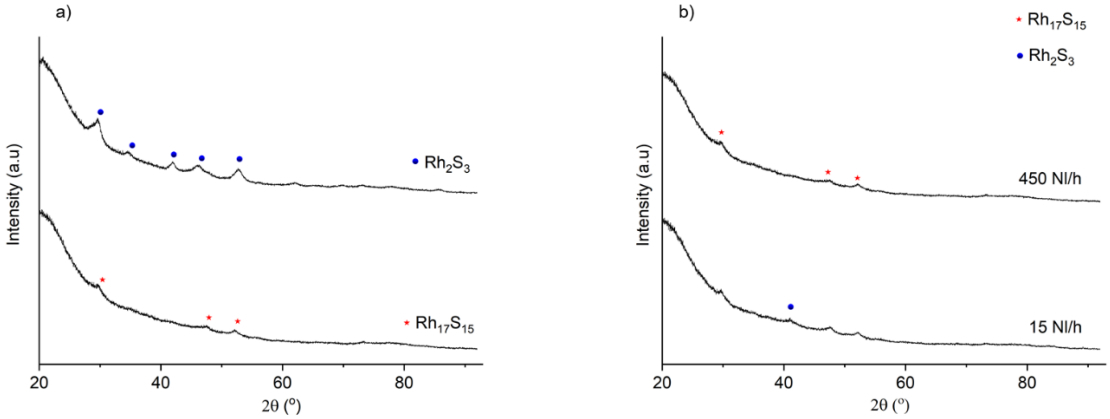


**Figure 1:** PXRD patterns of a) $Rh_{17}S_{15}/SiO_2$ (10 wt.% Rh) and $Rh_2S_3/SiO_2$ (10 wt.% Rh), b) products obtained after the thermal treatment at 700°C of the impregnated precursors for the synthesis of $Rh_{17}S_{15}/SiO_2$ (10 wt.% Rh) using different argon flow rates. •$Rh_2S_3$ (ICSD: 56882, Materials Project: mp-17173), *$Rh_{17}S_{15}$ (ICSD: 410838, Materials Project: mp-21991)

The phase purity of $Rh_{17}S_{15}/SiO_2$ (10 wt.% Rh) and $Rh_2S_3/SiO_2$ (10 wt.% Rh) can be verified by powder X-ray diffraction (PXRD) measurements (Figure 1a), whereby the occurrence of very broad reflexes already indicates the formation of small Rh-S crystallites. Subsequently, selected area electron diffraction (SAED) measurements in association with transmission electron microscopy (TEM) were performed for a detailed analysis and do provided evidence of the nanoparticles of $Rh_{17}S_{15}$ and $Rh_2S_3$ supported on silica (Figure S9 and S10). Despite the fact, that PXRD and SAED measurements can be applied for the analysis of the 10 wt.% loaded samples, the analyses of the samples resulting from a 1wt.% Rh loading, was found to be challenging due to the very small crystallite/particle sizes of the resulting rhodium sulphides particles (Figure S3). Interestingly, when $Rh/SiO_2$ (1 wt.% Rh) as reference system was prepared and analyzed via PXRD, reflexes corresponding to metallic Rh particles of large crystallite site can be identified despite the low metal loading (Figure S4). This already indicates the role of sulphur as inherent stabilization agent against sintering processes. The phase purity and integrity of all samples of rhodium sulphides, could, however, be proven by elemental mapping via energy dispersive X-ray spectroscopy (EDXS), irrespective of whether a high or low Rh loading was chosen. Hereby a uniform Rh and S distribution over silica, with S/Rh ratios of 0.9 for $Rh_{17}S_{15}/SiO_2$ (1 and 10 wt.% Rh) and 1.5 for the $Rh_2S_3/SiO_2$ (1 and 10 wt.% Rh, Figure 2 and Figures S11-S15), was obtained. Also, lattice fringe distances extracted through high resolution transmission electron microscopy (HR-TEM) for the $Rh_xS_y/SiO_2$ samples (x=17, y=15 or x=2, y=3 with 1 and 10 wt.% Rh) were well suited with the theoretical d spacing of the targeted rhodium sulphide phases (Figure S11-S15).

The morphology of the supported rhodium sulphide nanoparticles could be further explored by transmission electron microscopy. The TEM images of $Rh_xS_y/SiO_2$ (x=17, y=15 or x=2, y=3 with 1 and 10 wt.% Rh) show well dispersed rhodium sulphide nanoparticles on the support (Figure S11-S15) and example images of $Rh_{17}S_{15}/SiO_2$ with higher and lower Rh loadings are provided as Figure 2a and 2b. Almost spherical shaped nanoparticles can be observed in high angle annular dark field scanning transmission electron microscopy (HAADF-STEM) images (Figure S11-S15) of $Rh_xS_y/SiO_2$ (x=17, y=15 or x=2, y=3 with 1 and 10 wt.% Rh). Average particle sizes of 2.2 nm and 3.0 nm were determined for $Rh_{17}S_{15}/SiO_2$ (1 wt.% Rh) and $Rh_2S_3/SiO_2$ (1 wt.% Rh), whereas for the materials with a higher metal loading (10 wt.% Rh), particle sizes of 6.3 nm and 3.6 nm were observed. The increase in particle size due to higher metal loadings is attributed to the enhanced sintering at higher metal and sulphur precursor concentrations on the support[31] (Figure S7d and S8c). Interestingly, the high resolution HAADF-STEM images of $Rh_{17}S_{15}/SiO_2$ (10 wt.% Rh) through Z contrasting, indicate the formation of a Rh-based motif comprising of four adjacent Rh atoms (Figure 2c and d). Such structural motifs or ensembles on catalysts surfaces have been identified as active sites for several occasions in the field of heterogeneous catalysis,[32] whereby the Lindlar catalyst (typically 5 wt.% palladium deposited on calcium carbonate or barium sulfate and treated with various forms of lead),[33] is the prototypic example. Combined experimental and theoretical[34,35] work has shown that through the alloying of Pd with Pb, Pb induced exclusion areas and consequently triangular shaped active sites are formed, which are very active in the semi hydrogenation of alkynes[36]. The concept of well-defined structural motifs of crystalline alloys and intermetallic compounds can be also be witnesses beyond the Lindlar catalyst. For instance, an exceptional performance in alkyne semi hydrogenation has been attributed to spatially isolated metal trimers in $Pd_3S$[26] and $Ni_xP_y$[37].

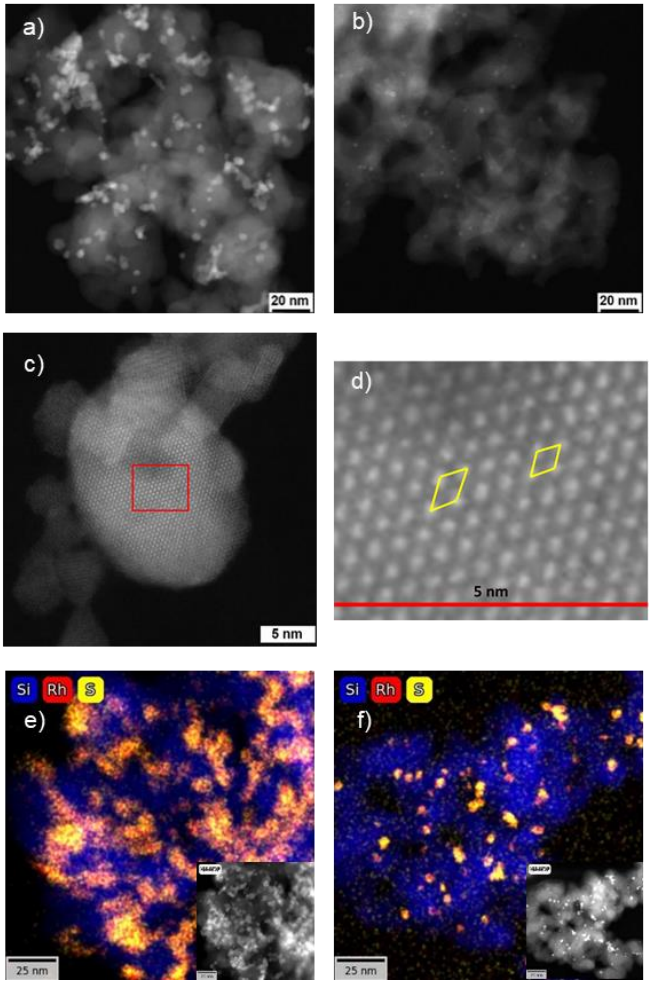


**Figure 2:** HAADF-STEM images of a) $Rh_{17}S_{15}/SiO_2$ (10 wt.% Rh) and b) $Rh_{17}S_{15}/SiO_2$ (1 wt.% Rh). c) HR-HAADF-STEM image of $Rh_{17}S_{15}/SiO_2$ (10 wt.% Rh) and d) magnified image highlighting the rhodium-containing structural motif. e) EDXS elemental mapping of Rh, S and Si for $Rh_{17}S_{15}/SiO_2$ (10 wt.% Rh) and f) $Rh_{17}S_{15}/SiO_2$ (1 wt.% Rh) with corresponding HAADF STEM images as insert.

To investigate the oxidation state of Rh within the supported rhodium sulphides, X ray photoelectron spectroscopy (XPS) analyses of $Rh_xS_y/SiO_2$ (x=17, y=15 or x=2, y=3 with 1 and 10 wt.% Rh) samples were conducted (Figure S20-23, Table S1-S3). Hereby, the Rh 3d signals were deconvoluted indicating the presence of two types of rhodium species. The doublet at binding energies of 309.5 eV and 314.4 eV corresponds to $3d_{5/2}$ and $3d_{3/2}$ states, which can be assigned to rhodium sulphide, as the signal at 309.5 eV is generally associated with covalently bonded Rh in an oxidized form[27,38]. This in combination with the sulphur 2p signals, seen in $Rh_xS_y/SiO_2$ (x=17, y=15 or x=2, y=3 with 10 wt.% Rh), at 161.7 eV and 162.7 eV, corresponding to polysulphides, points towards covalently bound rhodium and sulphur[27,38]. Further, no S 2p signals at 164 eV were observed, which proves the absence of any elemental sulphur.[27] Another doublet of Rh 3d observed at 307.5 eV ($3d_{5/2}$) and 312.2 eV ($3d_{3/2}$) corresponds to metallic rhodium Rh(0). The existence of $Rh^{\delta+}$ and $Rh^0$ species from XPS analyses has also been shown for $Rh_xP_y$ systems and can be

considered a typical feature for rhodium/p-block element-based phases[21]. Further, a rhodium to sulphur ratio of 1.11 was obtained for $Rh_{17}S_{15}/SiO_2$ (10 wt.% Rh) and 0.53 for $Rh_2S_3/SiO_2$ (10 wt.% Rh) (Table S3), which is in line with Rh to S ratios considering the stoichiometry of the phases. The XPS analyses of the low Rh content $Rh_xS_y/SiO_2$ (x=17, y=15 or x=2, y=3 with 1 wt.% Rh) materials have also shown the presence of $Rh^{\delta+}$ and $Rh^0$, however, no sulphur signals could be witnesses, due to the very low chalcogenide concentration.

The surface chemistry of the supported rhodium sulphides was further investigated via diffuse reflectance infrared Fourier transform spectroscopy (DRIFTS) using CO as probe molecule[39] (Figure 3 and S18). In the DRIFT spectra of $Rh_{17}S_{15}/SiO_2$ (1wt.% Rh, Figure 3a), the band observed at 2105 $cm^{-1}$ in the initial scan can be assigned to symmetric stretching modes of rhodium gem-dicarbonyl species ($Rh^{3+}(CO)_2$), whereas the signal at 2067 $cm^{-1}$ corresponds to linearly bound CO on metallic Rh ($Rh^0$-CO)[40,41]. On further exposure to CO, the signal at 2105 $cm^{-1}$ shifts to 2102 $cm^{-1}$ and can be assigned to positively charged rhodium coordinated to CO, $Rh^{\delta+}(CO)_2$. This reduction under CO atmosphere is also demonstrated by the appearance of the signal at 2036 $cm^{-1}$, which can be traced back to asymmetric $Rh^{\delta+}(CO)_2$ stretching modes. Similar observations were made for the DRIFT spectra of the rhodium lean material $Rh_2S_3/SiO_2$ (1wt.% Rh). Again, a signal at 2104 $cm^{-1}$ can be assigned to symmetric CO stretching modes of $Rh^{3+}(CO)_2$. Upon CO exposure, an immediate emergence of signals at 2086 $cm^{-1}$ and 2036 $cm^{-1}$ can be witnessed, which underlines the facile reducibility of the $Rh_2S_3$ surface species in contrast to $Rh_{17}S_{15}$. In order to elucidate the effect of the sulphur incorporation into rhodium in more detail, the CO adsorption behavior of $Rh/SiO_2$ (1 wt.% Rh) as reference system was investigated via DRIFTS measurements. Already before, the infrared vibration spectra of adsorbed CO has previously found to be different in sulfided compared to unsulfided rhodium materials[42–44]. In our case it became obvious that there is a blue shift of the symmetric and asymmetric stretches of rhodium gem-dicarbonyl species ($Rh(CO)_2$)[41] from pure Rh samples (2098 and 2028 $cm^{-1}$) to $Rh_{17}S_{15}$ (2102 $cm^{-1}$ and 2036 $cm^{-1}$). This finding can be attributed to a charge transfer from Rh to S, also demonstrated by XPS analyses, which leads to an increase in the cationic nature of the rhodium centers in rhodium sulphides in comparison to the pure metal[21]. Consequently, a destabilization of the CO adsorption is taking place, due to the weak electron back donation of cationic Rh species to the $\pi^*$ CO orbitals. The band observed at 1936 $cm^{-1}$ in $Rh/SiO_2$ (1 wt.% Rh) corresponds to a bridged CO vibration mode. Similar signals in this range are absent in the DRIFT spectra of $Rh_xS_y/SiO_2$ (x=17, y=15 or x=2, y=3 with 1 wt.% Rh), which points towards the existence of isolated CO chemisorption sites on the surface,[45] as already indicated from TEM imaging.

The oxidation state and chemical environment of the rhodium sulphides materials was further investigated using X ray absorption spectroscopy (XAS). The X ray absorption near edge structure (XANES) measurements (Figure 3d) show that the Rh centers within rhodium sulphides ($Rh_xS_y/SiO_2$, x=17, y=15 or x=2, y=3 with 1 wt.% Rh) seem to have a very similar oxidation state, that lays between the $Rh^{3+}$ state of bulk $Rh_2O_3$ and $Rh^0$ of the bulk Rh reference. This basically

corresponds to an oxidation state of $Rh^{\delta+}$ based on the partial charge transfer from Rh to S in rhodium sulphide samples, as already concluded before from XPS and DRIFTS analyses. The characteristic broad white line around 23240 eV observed in the XANES data was already reported for diverse $Rh_XS_Y$ species[46–48]. The corresponding Fourier transformed extended X-ray absorption fine structure (FT-EXAFS) spectra are plotted in Figure 3e and prove the existence of rhodium sulphides phases. However, in addition to the dominant main feature at a backscattering distance of 1.8 Å, which resembles Rh-S contributions, a shoulder at 1.5 Å could be observed. This shoulder corresponds to Rh-O, which most likely is due to the surface oxidation caused by the sample preparation and prolonged storage in ambient conditions in a capillary prior to the XAS measurements. In addition to these signals, a scattering event at a distance of 2.3 Å was observed in $Rh_{17}S_{15}/SiO_2$ (1 wt.% Rh), which can be attributed to Rh-Rh scattering events. This finding underlines the metal rich character of the $Rh_{17}S_{15}$ phase in contrast to the metal lean $Rh_2S_3$ counterpart and undermines the formation of Rh-containing single sites, as shown in Figure 2d.

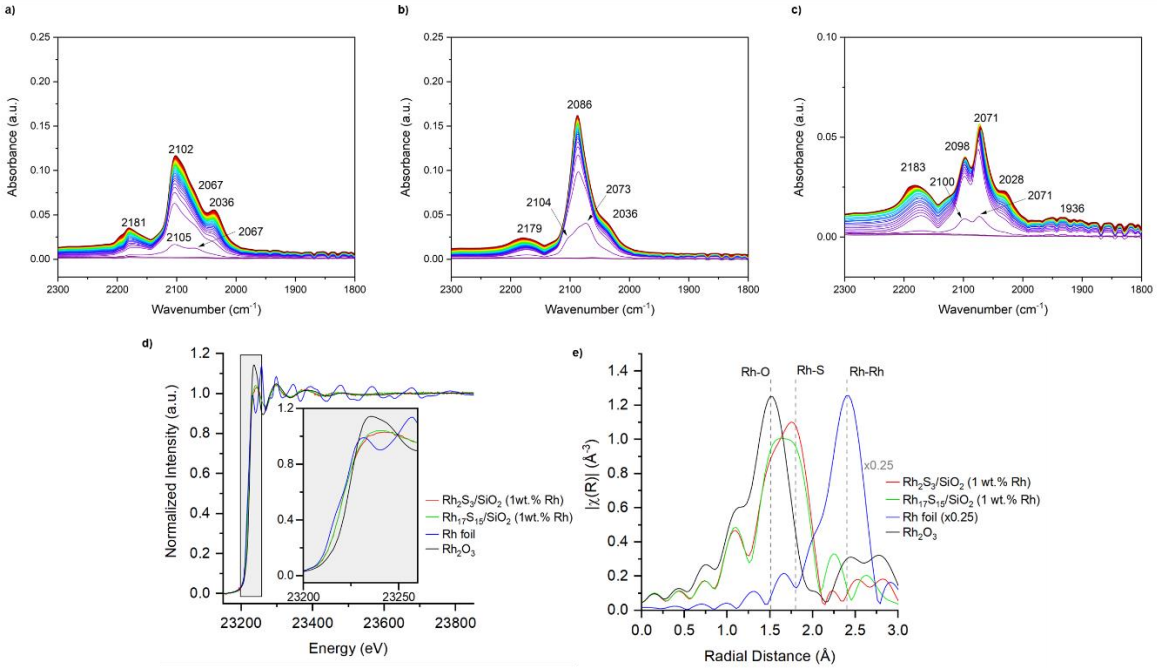


**Figure 3:** CO adsorption DRIFT spectra of the synthesized catalyst a) $Rh_{17}S_{15}/SiO_2$ (1wt.% Rh), b) $Rh_2S_3/SiO_2$ (1 wt.% Rh) and c) $Rh/SiO_2$ (1 wt.% Rh). Signals in the region of 2179 $cm^{-1}$ to 2183 $cm^{-1}$ correspond to free CO. (d) Ex situ XAS spectra recorded at the Rh-K edge with an inset showing the XANES region and e) FT-EXAFS spectra ($k^2$-weighted). As references, the spectra of a Rh foil and a $Rh_2O_3$ pellet are shown.

## Rhodium sulphides as heterogeneous hydroformylation catalysts

To assess the catalytic activity of supported rhodium sulphides nanoparticles in the hydroformylation of alkenes, styrene was selected as model substrate. During the

hydroformylation reaction of styrene with CO and $H_2$, the linear 3-phenylpropanal and branched 2-phenylpropanal aldehydes, as well as the undesired hydrogenation side product ethyl benzene can be formed[49]. Hereby, the modulation of the catalytic selectivity towards the aldehyde products and the therewith the reduction of the hydrogenation side reaction is one of the major goals in the development of hydroformylation catalysts[17].

**Table 1:** Hydroformylation of styrene using different supported rhodium sulphide catalysts.

| Entry | Catalyst | Rh loading (wt.%) | Reaction time (min) | Conversion (%) | Aldehyde selectivity (%) | n/iso |
|---|---|---|---|---|---|---|
| 1 | $Rh_{17}S_{15}/SiO_2$ | 10 | 80 | 18 | 100 | 0.7 |
| 2 | $Rh_2S_3/SiO_2$ | 10 | 80 | 5 | 100 | - |
| 3 | $Rh_{17}S_{15}/SiO_2$ | 10 | 225 | 85 | 99.3 | 0.88 |
| 4 | $Rh_2S_3/SiO_2$ | 10 | 225 | 42 | 100 | 0.7 |
| 5 | $Rh_{17}S_{15}/SiO_2$ | 1 | 80 | 87 | 98.4 | 0.85 |
| 6 | $Rh_{17}S_{15}/SiO_2$ | 1 | 180 | 100 | 97.3 | 1.0 |
| 7 | $Rh_2S_3/SiO_2$ | 1 | 80 | 60 | 98.7 | 0.85 |
| 8 | $Rh_2S_3/SiO_2$ | 1 | 120 | 93 | 98.6 | 0.85 |
| 9 | $Rh/SiO_2$ | 1 | 80 | 40 | 98.8 | 0.91 |

Reaction conditions: 1 mmol styrene, 1.5 mL toluene, 0.2 mol% catalyst, 40 bar syngas pressure, CO: $H_2$ 1:1, 80°C, 1200 rpm stirring speed.

Initial tests were performed using $Rh_{17}S_{15}/SiO_2$ (10 wt. % Rh) and $Rh_2S_3/SiO_2$ (10 wt. % Rh) as catalysts under a syn gas pressure of 40 bar (CO:$H_2$ 1:1) and a temperature of 80°C. The conversions of styrene after 80 mins of reaction time using $Rh_{17}S_{15}$ and $Rh_2S_3$ were 18% and 5% (Table 1, entry 1 and 2), respectively. An extended reaction time of 225 min resulted in higher conversions of 85% for $Rh_{17}S_{15}$ and 42% for $Rh_2S_3$ (Table 1, entry 3 and 4) with trace (1%) or no hydrogenation products. The regioselectivity expressed in terms of linear to branched aldehyde (n/iso) ratios were observed to be 0.88 and 0.7 for $Rh_{17}S_{15}$ and $Rh_2S_3$ respectively at the indicated conversions (Table 1, entry 3 and 4). Subsequently, rhodium sulphide catalysts prepared with 1 wt.% Rh loading on silica, were tested under similar reactions conditions. After 80 mins reaction time a styrene conversion of 87% was observed using $Rh_{17}S_{15}/SiO_2$ (1 wt.% Rh) as catalyst, whereas $Rh_2S_3/SiO_2$ (1 wt.% Rh) gave 60% conversion. From the above results, a superior activity of the metal rich $Rh_{17}S_{15}$ catalyst in comparison to $Rh_2S_3$ and a tremendous activity improvement at lower metal loadings can be concluded. The difference in activity of various phases and metal

loading is also visible in the plot of the syn gas pressure consumption in the reactor (Figure 4c), whereby a faster drop in absolute pressure was observed for $Rh_{17}S_{15}/SiO_2$ (1 wt.% Rh) compared to other rhodium sulphide catalysts. The enhanced performance of the catalyst with lower Rh loadings may be due to the reduced particle size and resulting higher rhodium dispersion as concluded from the TEM analysis (Figure S7 and S8). We assume that lower metal loadings in the synthesis lead to an increased number of exposed surface atoms on the support and available active sites[50]. The conversion vs time plot (Figure 4d) also clearly emphasize the better performance of $Rh_{17}S_{15}/SiO_2$ (1 wt.% Rh) in terms of activity. A reaction time of 3h using $Rh_{17}S_{15}/SiO_2$ (1 wt.% Rh) as catalyst resulted in 100% conversion of styrene (Table 1, entry 6) with an n/iso ratio of 1.0 and a hydrogenation product concentration of only 2.7% (ethyl benzene). The catalytic activity of pure Rh on silica (1 wt.% Rh) was investigated as reference point and it could be shown that both rhodium sulphide based catalysts show superior catalytic activity. Similar observations were reported for sulphided rhodium in gas phase hydroformylation reactions[40,43], however, no systematic investigation of the catalytically active phases and the influence of the sulphur incorporation of the steric and electronic parameters were carried out in the work reported. From the above results an order of activity towards hydroformylation of styrene can be concluded as follows: $Rh<Rh_2S_3<Rh_{17}S_{15}$.

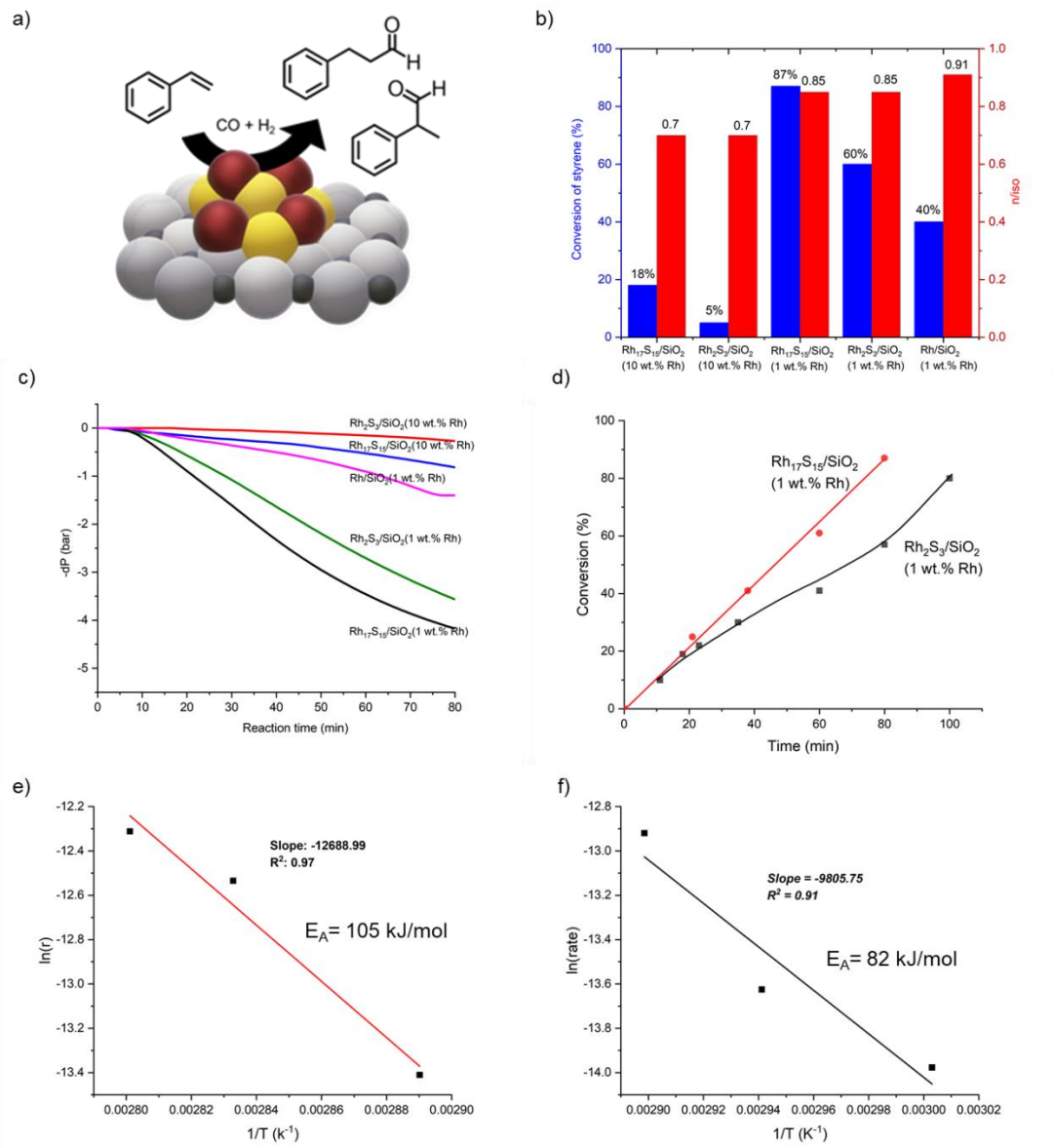


**Figure 4:** a) Schematic representation of styrene hydroformylation using silica supported rhodium sulphide catalysts (red: Rh, yellow: S), b) chart showing the conversion and selectivity after 80 min reaction time, c) pressure loss of synthesis gas inside the reactor at 80°C, d) conversion vs time plot using $Rh_xS_y/SiO_2$ (x=17, y=15 or x=2, y=3 with 1 wt.% Rh) catalysts at 80°C, e) Arrhenius plot for the estimation of the activation energy with $Rh_2S_3/SiO_2$ (1 wt.% Rh) as catalyst and f) with $Rh_{17}S_{15}/SiO_2$ (1 wt.% Rh). Hydroformylation reaction conditions: 1 mmol styrene, 1.5 mL toluene, 0.2 mol% catalyst, 40 bar syngas pressure, CO: $H_2$ 1:1, 1200 rpm stirring speed.

The turn over frequency (TOF) values for the hydroformylation of styrene at 80°C and 40 bar syngas pressure were estimated as 2620 $h^{-1}$ for $Rh_{17}S_{15}/SiO_2$ (1 wt.% Rh) and 1450 $h^{-1}$ for $Rh_2S_3/SiO_2$ (1 wt.% Rh). These estimations were performed based on the metal dispersion calculated by the average particle diameter obtained from TEM imaging (Table S10). A comparison of TOF values under similar reaction conditions has shown a superior TOF value for $Rh_{17}S_{15}/SiO_2$ (2621 $h^{-1}$, 1 wt.% Rh) in comparison to $Rh_2P/SiO_2$ (1469 $h^{-1}$)[21] and $Rh_7Co_1P_4/SiO_2$ (2563 $h^{-1}$),[51] underlining the advanced performance of our lead catalyst candidate (Table S10 and Figure 5).

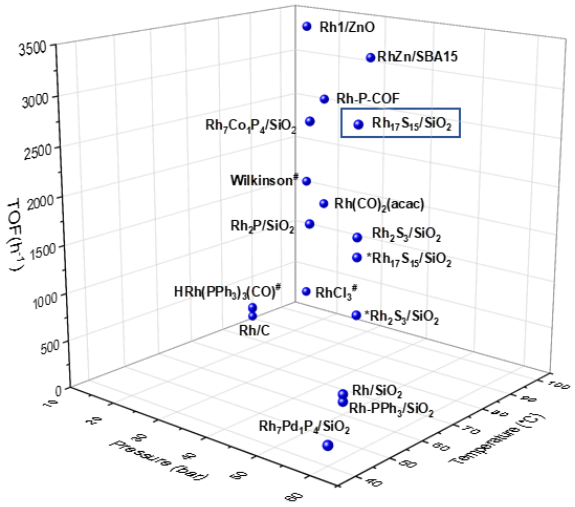


**Figure 5:** Schematic representation of the comparison of various TOF values reported for different heterogeneous hydroformylation catalysts applied in the hydroformylation of styrene.[4,12,13,21,51–54] *Estimation based on total Rh content. #Homogeneous catalyst.

The apparent activation energies of the supported rhodium sulphide catalyzed styrene hydroformylation reactions were estimated by Arrhenius plots (Figure 3 and S27). A higher apparent activation energy of 105 kJ/mol was estimated for $Rh_2S_3/SiO_2$ (1 wt.% Rh) in comparison to 82 kJ/mol for $Rh_{17}S_{15}/SiO_2$ (1 wt.% Rh), it can be argued that the findings are in line with the observed activity differences of these phases. Activation energies of styrene hydroformylation reported for other rhodium-based catalysts are provided in Table S9 and the values indicated a comparable performance of $Rh_{17}S_{15}/SiO_2$ (1 wt.% Rh). For example, the activation energy associated with other Rh-p block element combination phases, namely supported $Rh_2P$, is reported to be 71.4 kJ/mol[21], which indicates the analogues performance with the lead candidate of this work $Rh_{17}S_{15}/SiO_2$ (1wt.% Rh). This again undermines the hypothesis that the d block–p block combination strategy, through the electronic and steric modulation of the metal matrix, is a facile approach in mimicking metal ligand complexes employed in homogeneous catalysis.

The temperature dependency of the hydroformylation was further investigated by assessing the conversion and selectivity over the course of the reaction using $Rh_{17}S_{15}/SiO_2$ (1 wt.% Rh) as lead

catalyst candidate. An improved conversion of styrene beside a higher selectivity towards the linear aldehyde (improved n/iso) can be observed with increasing reaction temperature (Figure S28). In the accepted reaction mechanisms for the hydroformylation reaction, the formation of the branched versus the linear alkyl-rhodium complex is the crucial point for the regioselectivity determining step[14]. High temperatures (thermodynamic control) favour the isomerization of the branched alkyl-Rh complex to the linear alkyl-Rh species, thereby increasing the linear aldehyde selectivity[55,56]. The catalytic behavior on variation of the CO to $H_2$ ratio was again investigated using $Rh_{17}S_{15}/SiO_2$ (1 wt.% Rh) as lead catalyst candidate. Hereby an enhanced styrene conversion was observed with equal partial pressures of $H_2$ and CO (Figure S29), whereas a higher $H_2$ partial pressure (CO:$H_2$ 1:4) leads to an increased hydrogenation (4.7% ethyl benzene at 80% conversion). To broaden the application scope of the catalysts, also with respect to industrially relevant conditions, hydroformylation reactions without additional solvent were carried out. Hereby it was found that by using the lead catalyst candidate $Rh_{17}S_{15}/SiO_2$ (1 wt.% Rh) also 40% conversion in 120 min could achieved in neat styrene (Table S7). Further, the substrate scope was extended, and the lead catalyst candidate has shown to be active in the hydroformylation of 1-hexane, 1-octene, 2-octene and allyl benzene showing excellent activities and selectivity's towards the aldehydes (Table S6). Hereby, a comparable and even superior performance to some of the most active heterogeneous Rh-based hydroformylation catalysts was observed comparing $Rh_{17}S_{15}/SiO_2$ (1 wt.% Rh) in the hydroformylation of 1-hexene against other candidate materials (Table S8). For instance, Rh-$PPh_3/C$[18] and Rh/C[18] with 1 wt.% Rh loading on the support have shown 100% and 63% 1-hexene conversion in 5h with 83% and 72% selectivity, respectively, towards the aldehydes, whereas $Rh_{17}S_{15}/SiO_2$ (1 wt.% Rh) exhibited 100% conversion with an aldehyde selectivity of 92% in 4 h reaction time.

To explore the recyclability of the supported rhodium sulphide catalysts, $Rh_{17}S_{15}/SiO_2$ (1 wt.% Rh) and $Rh_2S_3/SiO_2$ (1 wt.% Rh) were recovered after the hydroformylation reaction by centrifugation and have been reused in the hydroformylation of styrene. This recovery confirmed the reusability of the catalysts, as no decline in activity or selectivity (n/iso consistently in the range 0.85 to 0.9) was observed for the catalysts even after two rounds of recycling (Figure S31). With $Rh_{17}S_{15}/SiO_2$ (1 wt.% Rh) providing a reaction time for 80 min, a styrene conversion of 87% was observed with the fresh catalyst and a slightly higher conversion of 94% in the second round of recycling. Similarly, after a reaction time of 120 min using the fresh $Rh_2S_3/SiO_2$ (1 wt.% Rh) catalysts a conversion of 93% could be achieved, whereas 97% of styrene conversion were obtained in the second round of recycling. However, ICP AES analysis of the recovered catalyst showed a Rh loss (from 1.02 wt.% to 0.78 for $Rh_{17}S_{15}/SiO_2$, 1 wt.% Rh and from 0.88 wt.% to 0.73 wt.% for $Rh_2S_3/SiO_2$, 1 wt.% Rh, Table S11) along with a reduction in the Si content, which points towards a mechanical decomposition of the catalyst. Similar observations were made for other Rh-based hydroformylation catalysts,[49] and show the importance of tailoring the metal-support interactions.[57] In addition to the elemental analysis of postreaction samples, the recovered catalysts were also analyzed via TEM imaging to identify if any changes have occurred to the particles during the catalytic reaction (Figure S16 and S17). The HAADF STEM images (Figure S17 and

S16) of the recovered $Rh_{17}S_{15}/SiO_2$ (1 wt.% Rh) and $Rh_2S_3/SiO_2$ (1 wt.% Rh) samples showed well dispersed rhodium sulphide nanoparticles on the silica support. Lattice fringe d spacing of 0.2115 nm in line with $Rh_{17}S_{15}$ (400) and 0.2443 nm corresponding to $Rh_2S_3$ (220) were extracted for the recovered $Rh_{17}S_{15}/SiO_2$ (1 wt.% Rh) and $Rh_2S_3/SiO_2$ (1 wt.% Rh) catalysts from the HRTEM bright field images (Figure S17 and S16) and indicate the stability of $Rh_xS_y$ phases after the catalysis. The particle sizes, determined via TEM imaging with the aim to identify sintering or aggregations, revealed a slight increase in the average particle size for the recovered $Rh_{17}S_{15}/SiO_2$ sample (1 wt.% Rh) and substantial decrease in the case of $Rh_2S_3/SiO_2$ (1 wt.% Rh) (Table S12). The stability of the phase, besides a minor loss in crystallinity, was also proven be PXRD analysis of the recovered 10 wt.% Rh loaded $Rh_{17}S_{15}$ and $Rh_2S_3/SiO_2$ catalysts (Figure S5). The XAS analyses performed for the recovered $Rh_xS_y/SiO_2$ (x=17, y=15 or x=2, y=3 with 1 wt.% Rh) catalysts still indicates the $Rh^{\delta+}$ oxidation state based on the analyses of the XANES region (Figure S24). However, especially in the case of the sulphur rich phase $Rh_2S_3$, the signal at a backscattering distance of 2.3 Å in the FT-XAFS spectra has increased (Figure S25). This could imply a loss of sulphur and the partial phase transition from $Rh_2S_3$ into $Rh_{17}S_{15}$, which can also explain the slightly enhanced performance of the recovered $Rh_2S_3/SiO_2$ (1 wt.% Rh) catalyst in comparison to the fresh catalyst during the catalyst recycling study (Figure S31c).

**Computational modelling**

To gain further understanding of the remarkable performance of the synthetized catalysts, atomistic simulation was employed. Firstly, the local environment level atomic scale structural differences between the three key active phases $Rh_{17}S_{15}$, $Rh_2S_3$ and Rh were explored. The structure of metallic rhodium is well known with its cubic close-packed lattice. Regardless of the crystallographic orientation and termination of the exposed surface, Rh surfaces are comprised of Rh sites neighboured by other Rh sites. The spatial proximity of these metal sites and their chemical similarity allows for reaction intermediates of neighboring sites to interact which can lead to a compromised performance.[58]

In comparison to pure rhodium, both S containing materials offer much more structural diversity over the different terminations and crystallographic directions. Enumerating all surface terminations up to third Miller indices and identifying potential adsorption sites (active sites) for both $Rh_{17}S_{15}$ and $Rh_2S_3$, we found over 240.000 high symmetry options (using CATKIT)[59,60]. To visualize the structural diversity among active sites, SOAP[61] descriptors (with a 3.0 Å cutoff, i.e. including ~ 1 nearest neighbor sphere) were generated at each identified site and non linear dimensionality reduction with emphasis on proximity matching through t-SNE[62] was performed to derive a two dimensional visual representation[61,63–65] (Figure 6 a, b and c). Colored by S/Rh ratio, Rh content, and origin, we noticed that Rh rich and Rh poor sites exist for both materials at S/Rh ratios in the range from 1 to 6, and we could not identify distinct clusters of single origin, but we found non-overlapping domains. This indicates that a majority of sites (categorized by structural similarity) can exist on both materials, but not all. We further focus our efforts on identifying differences between the materials.

Looking into the surface concentrations of the full set of sites, the Rh rich material, $Rh_{17}S_{15}$, as expected, has a higher number or Rh rich surfaces, as shown in Figure 6d. The most prominent site in the $Rh_2S_3$ material is surrounded by 1 Rh and 2 S atoms (Figure 6e). In contrast, sites of $Rh_{17}S_{15}$ show higher variety in the composition of their first neighbor sphere with the most common site being comprised of 3 Rh atoms and 2 (or 1) S atoms.

As to what extent does the chemical behavior of the surfaces differ, we focused our attention to the most stable crystallographic directions[28], (001) for $Rh_2S_3$ and (100) for $Rh_{17}S_{15}$, as these span a comprehensive range of local site S to Rh ratios (Figure 6a, Figure 6g). A simple Rh(111) slab with an S add-atom was included as reference material. We considered all Rh containing sites for all terminations of these facets, from S rich (excess of surface S) to Rh rich (surface S depleted). The sampled sites cover the surface a local (in the primary neighborhood of the site) space well (Figure 6g). We find more variety in the local composition (composition defined by the number of atoms in a 3 Å radius, sum of the covalent radii of Rh: 1.3 Å and S: 1 Å) of the $Rh_{17}S_{15}$ sites that span local S/Rh ratios from ~0 to 6 as opposed to 1 to 5 in $Rh_2S_3$. We used DFT to compute the adsorption energy of CO ($E_{CO}$) to gage the chemical affinity towards one of the substrates of the hydroformylation reaction of these sites,[19] and again find the sites of $Rh_{17}S_{15}$ as outliers of the range (Figure 6h, Figure S33-S36). Going from a S saturated $Rh_{17}S_{15}$ termination to a S depleted surface we found a notable increase in CO affinity, from ~-1.3 eV (Figure 6h, purple) to bellow -2.25 eV (Figure 6h, brown). These values are even lower than on the reference S doped Rh slab (Figure 6h, light blue). In fact, the local site composition appears to have a profound impact on the CO affinity (Figure 6i) where the strongest binding sites were found to be pure Rh sites while the weakest were found to be Rh sites where Rh is surrounded by S. Thus, tuning the surface S/Rh ration of Rh sulfides unlocks a range of catalysts with distinct substrate affinities, particularly for $Rh_{17}S_{15}$, as its sites cover a wide range of energies.

An additional geometrical feature uncovered on the S poor terminations of the $Rh_{17}S_{15}$ material is the spatial resolution of neighboring $Rh_4$ sites. In contrast to metallic Rh, where Rh hollow sites are always available, or $Rh_2S_3$ where ‘pure’ (sites where the adsorbate has only Rh atoms as its first neighbors) Rh hollow sites are non-existent, Rh poor terminations of $Rh_{17}S_{15}$ effectively prevent all side reactions that require the participation of neighboring hollow sites (Figure S37). These $Rh_4$ sites can not only be found computationally for the lead catalyst $Rh_{17}S_{15}/SiO_2$, but we have also imaged them on an atomistic level using TEM. Further, XAS and DRIFTS analyses undermine the existence of isolated hollow sites.

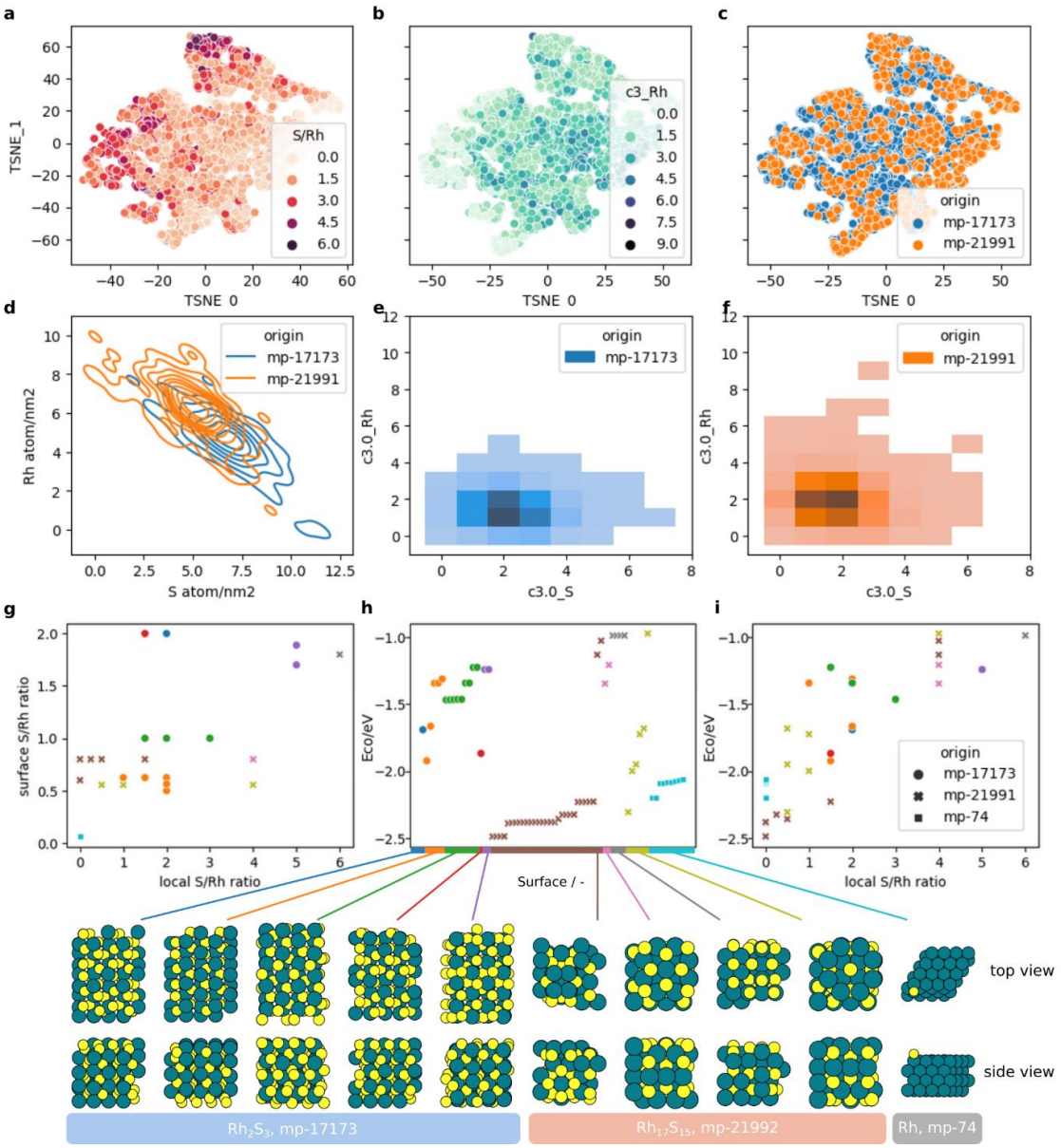


**Figure 6:** t-SNE of the SOAP representation of the (10.000 out of 240.000) enumerated sites on all terminations for all crystallographic directions up to miller index = 3 for $Rh_{17}S_{15}$ (mp-21991) and $Rh_2S_3$ (mp-17173), a) colored by the S to Rh ratio of atoms in a 3 Å radius of the site, b) colored by the number of Rh atoms in a 3 Å radius of the site, c) colored by the material origin, d) overview of the surface compositions of all enumerated surfaces and terminations, local composition of all numerated adsorption sites on e) $Rh_2S_3$ (mp-17173) and f) $Rh_{17}S_{15}$ (mp-21991), g) ratio of the number of surface atoms of S/Rh versus the local (within 3 Å of the adsorbate contact atom) S/Rh ratio, h) CO adsorption energy ($E_{CO} = E_{*CO} – E_{CO} – E_{*}$) plotted as a function of origin, i) CO adsorption energy plotted as a function of local composition. Inset bellow: top and side view of (100) $Rh_{17}S_{15}$ (mp-21991), (001) $Rh_2S_3$ (mp-17173) and S doped (111) Rh (mp-74) surfaces with different terminations. Rh (S) atoms shown as blue (yellow) spheres.

In conclusion, supported rhodium sulphides have demonstrated to be excellent catalysts for the hydroformylation of alkenes in the liquid phase, due to the high degree of catalytic surface tunability and the possible formation of highly reactive $Rh_4$ assembles with tailored geometric and electronic properties. These are accessible through a precisely controlled synthesis and subsequent thermal treatment procedure. This study shows that the d-block/p-block element combination strategy can be employed for a tailored engineering of metal matrices via the dilution with p-block elements and the subsequent formation of highly active heterogeneous catalysts.

**Acknowledgements**

We gratefully acknowledge funding for A.N. from BASF. We are also grateful for fruitful discussions within hte GmbH. Moreover, we would like to thank BASF for analytic measurements (Edith Rothermel, Thorsten Wieczorek and Dr. Philipp Müller for TEM and Dr. Sabine Hirth for XPS measurements). This study was also supported by the Deutsche Forschungsgemeinschaft (DFG, German Research Foundation) −SFB 1441− Project-ID 426888090. We would also like to thank the Institute for Beam Physics and Technology (IBPT) for the operation of the storage ring, the Karlsruhe Research Accelerator (KARA) as well as the KIT light source. Provision of instruments at the CAT-ACT beamline of KIT-ITCP together with the Institute of Nuclear Waste Disposal (INE) and help and technical support during the experiments by Dr. Anna Zimina (IKFT) is gratefully acknowledged. In addition, we would like to thank Prof. C. Feldmann and Prof. P. Roesky for their continuous support.

**Data availability statement**

The data that support the findings of this study are available within the electronic supplementary information. Additionally, a patent application (KIT, BASF SE) was filed.

## References


1. Liu, Y. *et al.* Rhodium nanoparticles supported on silanol-rich zeolites beyond the homogeneous Wilkinson's catalyst for hydroformylation of olefins. *Nat. Commun.* **14**, 2531 (2023).

2. Wang, L. *et al.* Atomic-level insights in optimizing reaction paths for hydroformylation reaction over Rh/CoO single-atom catalyst. *Nat. Commun.* **7**, 14036 (2016).

3. Franke, R., Selent, D. & Börner, A. Applied Hydroformylation. *Chem. Rev.* **112**, 5675–5732 (2012).

4. Amsler, J. *et al.* Prospects of Heterogeneous Hydroformylation with Supported Single Atom Catalysts. *J. Am. Chem. Soc.* **142**, 5087–5096 (2020).

5. Pedersen, S. K. *et al.* Main element chemistry enables gas-cylinder-free hydroformylations. *Nat. Catal.* **3**, 843–850 (2020).

6. You, C. *et al.* Silicon-oriented regio- and enantioselective rhodium-catalyzed hydroformylation. *Nat. Commun.* **9**, 2045 (2018).

7. Gao, P. *et al.* Phosphorus coordinated Rh single-atom sites on nanodiamond as highly regioselective catalyst for hydroformylation of olefins. *Nat. Commun.* **12**, 4698 (2021).

8. Zhao, M. *et al.* Low-temperature hydroformylation of ethylene by phosphorous stabilized Rh sites in a one-pot synthesized Rh-(O)-P-MFI zeolite. *Nat. Commun.* **14**, 7174 (2023).

9. Evans, D., Osborn, J. A. & Wilkinson, G. Hydroformylation of alkenes by use of rhodium complex catalysts. *J. Chem. Soc. A* 3133–3142 (1968).

10. Raghuvanshi, K. *et al.* Highly Efficient 1-Octene Hydroformylation at Low Syngas Pressure: From Single-Droplet Screening to Continuous Flow Synthesis. *ACS Catal.* **10**, 7535–7542 (2020).

11. Neto, D. H. C., Dos Santos, A. A. M., Da Silva, J. C. S., Rocha, W. R. & Dias, R. P. Propene Hydroformylation Reaction Catalyzed by HRh(CO)(BISBI): A Thermodynamic and Kinetic Analysis of the Full Catalytic Cycle. *Eur. J. Inorg. Chem.* **2020**, 3907–3916 (2020).

12. Lang, R. *et al.* Hydroformylation of Olefins by a Rhodium Single-Atom Catalyst with Activity Comparable to RhCl(PPh3)3. *Angew. Chemie Int. Ed.* **55**, 16054–16058 (2016).

13. Chen, M. *et al.* Intermetallic Nanocatalyst for Highly Active Heterogeneous Hydroformylation. *J. Am. Chem. Soc.* **143**, 20907–20915 (2021).

14. Hanf, S., Rupflin, L. A., Gläser, R. & Schunk, S. A. Current state of the art of the solid rh-based catalyzed hydroformylation of short-chain olefins. *Catalysts* **10**, 1–36 (2020).

15. Zhou, W., Li, Y. & He, D. Substrate influences on activity and stability of SBA-15–Pr-anchored Rh–P complex catalysts for olefin hydroformylation. *Appl. Catal. A Gen.* **377**, 114–120 (2010).

16. Samanta, P. *et al.* Heterogenized Molecular Rhodium Phosphine Catalysts within Metal–Organic Frameworks for Alkene Hydroformylation. *ACS Catal.* **13**, 4193–4204 (2023).

17. Alvarado Rupflin, L. *et al.* Platinum Group Metal Phosphides as Heterogeneous Catalysts for the Gas-Phase Hydroformylation of Small Olefins. *ACS Catal.* **7**, 3584–3590 (2017).

18. Galdeano-Ruano, C., Lopes, C. W., Motta Meira, D., Corma, A. & Oña-Burgos, P. Rh 2 P Nanoparticles Stabilized by Carbon Patches for Hydroformylation of Olefins. *ACS Appl. Nano Mater.* **4**, 10743–10753 (2021).

19. Mao, Z., Guo, H., Xie, Z., Liu, P. & Chen, J. G. Trends and descriptors of heterogeneous hydroformylation activity and selectivity of RhM3 (M = Fe, Co, Ni, Cu and Zn) catalysts. *Catal. Sci. Technol.* **12**, 4988–4992 (2022).

20. Huang, N., Liu, B., Lan, X. & Wang, T. Insights into the Bimetallic Effects of a RhCo Catalyst for Ethene Hydroformylation: Experimental and DFT Investigations. *Ind. Eng. Chem. Res.* **59**, 18771–18780 (2020).

21. Liu, B., Huang, N., Wang, Y., Lan, X. & Wang, T. Promotion of Inorganic Phosphorus on Rh Catalysts in Styrene Hydroformylation: Geometric and Electronic Effects. *ACS Catal.* **11**, 1787–1796 (2021).

22. Liu, B., Lan, X., Zhong, Q. & Wang, T. Metal Phosphide: An Atypical Catalytic Site. *ACS Catal.* **14**, 757–775 (2024).

23. Liu, C., Zhang, J., Liu, H., Qiu, J. & Zhang, X. Heterogeneous Ligand-Free Rhodium Oxide Catalyst Embedded within Zeolitic Microchannel to Enhance Regioselectivity in Hydroformylation. *Ind. Eng. Chem. Res.* **58**, 21285–21295 (2019).

24. Neyyathala, A., Flecken, F. & Hanf, S. A Supported Palladium Phosphide Catalyst for the Wacker-Tsuji-Oxidation of Styrene. *Chempluschem* **88**, e202200431 (2023).

25. Mao, Z., Xie, Z. & Chen, J. G. Comparison of Heterogeneous Hydroformylation of Ethylene and Propylene over RhCo 3 /MCM-41 Catalysts. *ACS Catal.* **11**, 14575–14585 (2021).

26. Albani, D. *et al.* Selective ensembles in supported palladium sulfide nanoparticles for alkyne semi-hydrogenation. *Nat. Commun.* **9**, 1–11 (2018).

27. Masud, J. *et al.* A Rh x S y /C Catalyst for the Hydrogen Oxidation and Hydrogen Evolution Reactions in HBr . *J. Electrochem. Soc.* **162**, F455–F462 (2015).

28. Singh, N. *et al.* Investigation of the active sites of rhodium sulfide for hydrogen evolution/oxidation using carbon monoxide as a probe. *Langmuir* **30**, 5662–5668 (2014).

29. Richards, D., Young, S. D., Goldsmith, B. R. & Singh, N. Electrocatalytic nitrate reduction on rhodium sulfide compared to Pt and Rh in the presence of chloride. *Catal. Sci. Technol.* **11**, 7331–7346 (2021).

30. Zhang, W., Yanagisawa, K., Kamiya, S. & Shou, T. Phase controllable synthesis of well-crystallized rhodium sulfides by the hydrothermal method. *Cryst. Growth Des.* **9**, 3765–

3770 (2009).

31. Yin, P. *et al.* Quantification of critical particle distance for mitigating catalyst sintering. *Nat. Commun.* **12**, 4865 (2021).

32. Vogt, C. & Weckhuysen, B. M. The concept of active site in heterogeneous catalysis. *Nat. Rev. Chem.* **6**, 89–111 (2022).

33. Lindlar, H. Ein neuer Katalysator für selektive Hydrierungen. *Helv. Chim. Acta* **35**, 446–450 (1952).

34. Studt, F. *et al.* Identification of non-precious metal alloy catalysts for selective hydrogenation of acetylene. *Science* **320**, 1320–1322 (2008).

35. Studt, F. *et al.* On the Role of Surface Modifications of Palladium Catalysts in the Selective Hydrogenation of Acetylene. *Angew. Chemie Int. Ed.* **47**, 9299–9302 (2008).

36. Vilé, G., Almora-Barrios, N., Mitchell, S., López, N. & Pérez-Ramírez, J. From the Lindlar Catalyst to Supported Ligand-Modified Palladium Nanoparticles: Selectivity Patterns and Accessibility Constraints in the Continuous-Flow Three-Phase Hydrogenation of Acetylenic Compounds. *Chem. – A Eur. J.* **20**, 5926–5937 (2014).

37. Albani, D. *et al.* Ensemble Design in Nickel Phosphide Catalysts for Alkyne Semi-Hydrogenation. *ChemCatChem* **11**, 457–464 (2019).

38. Li, Y., Li, N., Yanagisawa, K., Ding, X. & Li, X. In situ synthesis of well crystallized rhodium sulfide/carbon composite nanospheres as catalyst for hydrochloric acid electrolysis. *J. Mater. Chem. A* **2**, 1484–1492 (2014).

39. Sarma, B. B. *et al.* Tracking and Understanding Dynamics of Atoms and Clusters of Late Transition Metals with In-Situ DRIFT and XAS Spectroscopy Assisted by DFT. *J. Phys. Chem. C* **127**, 3032–3046 (2023).

40. Srinivas, G. & Chuang, S. S. C. An in-Situ Infrared Study of the Formation of n- and iso-Butyraldehyde from Propylene Hydroformylation on Rh/SiO2 and Sulfided Rh/SiO2. *J. Catal.* **144**, 131–147 (1993).

41. Niemantsverdriet, J. W. *Spectroscopy in Catalysis: An Introduction, 2nd, Completely Revised Edition*. (Wiley-VCH Verlag, 2000).

42. Chuang, S. S. C. & Pien, S. I. Infrared study of the CO insertion reaction on reduced, oxidized, and sulfided Rh/SiO2 catalysts. *J. Catal.* **135**, 618–634 (1992).

43. Konishi, Y., Ichikawa, M. & Sachtler, W. M. H. Hydrogenation and hydroformylation with supported rhodium catalysts. Effect of adsorbed sulfur. *J. Phys. Chem.* **91**, 6286–6291 (1987).

44. Mills, P., Phillips, D. C., Woodruff, B. P., Main, R. & Bussell, M. E. Investigation of the Adsorption and Reactions of Thiophene on Sulfided Cu, Mo, and Rh Catalysts. *J. Phys. Chem. B* **104**, 3237–3249 (2000).

45. Meunier, F. C. Relevance of IR Spectroscopy of Adsorbed CO for the Characterization of Heterogeneous Catalysts Containing Isolated Atoms. *J. Phys. Chem. C* **125**, 21810–21823 (2021).

46. Ziegelbauer, J. M. *et al.* Fundamental Investigation of Oxygen Reduction Reaction on Rhodium Sulfide-Based Chalcogenides. *J. Phys. Chem. C* **113**, 6955–6968 (2009).

47. Liang, J. *et al.* Reactivity and Transformation of Antimetastatic and Cytotoxic Rhodium(III)–Dimethyl Sulfoxide Complexes in Biological Fluids: An XAS Speciation Study. *Inorg. Chem.* **58**, 4880–4893 (2019).

48. Mukerjee, S., Ramaker, D., Gatewood, D. & Ziegelbauer, J. M. In Situ X-Ray Absorption Spectroscopy Studies of Water Activation on Novel Electrocatalysts for Oxygen Reduction Reaction in Acid Electrolyte. *ECS Trans.* **1**, 119–128 (2006).

49. Li, T. *et al.* Styrene Hydroformylation with In Situ Hydrogen: Regioselectivity Control by Coupling with the Low-Temperature Water–Gas Shift Reaction. *Angew. Chemie Int. Ed.* **59**, 7430–7434 (2020).

50. Bano, A. *et al.* Enhancing catalytic activity of gold nanoparticles in a standard redox reaction by investigating the impact of AuNPs size, temperature and reductant concentrations. *Sci. Rep.* **13**, 12359 (2023).

51. Liu, B., Wang, Y., Huang, N., Lan, X. & Wang, T. Activity Promotion of Rh8-xCoxP4Bimetallic Phosphides in Styrene Hydroformylation: Dual Influence of Adsorption and Surface Reaction. *ACS Catal.* **11**, 9850–9859 (2021).

52. Liu, Y. *et al.* Triphenylphosphine-Based Covalent Organic Frameworks and Heterogeneous Rh-P-COFs Catalysts. *Chem. – A Eur. J.* **26**, 12134–12139 (2020).

53. Han, D. *et al.* Asymmetric hydroformylation of olefins catalyzed by rhodium nanoparticles chirally stabilized with (R)-BINAP ligand. *J. Mol. Catal. A Chem.* **283**, 15–22 (2008).

54. Liu, B., Huang, N., Wang, Y., Lan, X. & Wang, T. Regioselectivity regulation of styrene hydroformylation over Rh-based Phosphides: Combination of DFT calculations and kinetic studies. *Chem. Eng. J.* **441**, 136101 (2022).

55. Lazzaroni, R., Raffaelli, A., Settambolo, R., Bertozzi, S. & Vitulli, G. Regioselectivity in the rhodium-catalyzed hydroformylation of styrene as a function of reaction temperature and gas pressure. *J. Mol. Catal.* **50**, 1–9 (1989).

56. Güven, S. *et al.* Kinetic Explanation for the Temperature Dependence of the Regioselectivity in the Hydroformylation of Neohexene. *ChemCatChem* **6**, 603–610 (2014).

57. Neyyathala, A., Flecken, F., Rang, F., Papke, C. & Hanf, S. Support Engineering for the Stabilisation of Heterogeneous Pd3P-Based Catalysts for Heck Coupling Reactions. *Chem. – A Eur. J.* **30**, e202302825 (2024).

58. García-Mota, M. *et al.* A density functional theory study of the 'mythic' Lindlar hydrogenation catalyst. *Theor. Chem. Acc.* **128**, 663–673 (2011).

59. Bartók, A. P., Kondor, R. & Csányi, G. On representing chemical environments. *Phys. Rev. B* **87**, 184115 (2013).

60. Himanen, L. *et al.* DScribe: Library of descriptors for machine learning in materials science. *Comput. Phys. Commun.* **247**, 106949 (2020).

61. De, S., Bartók, A. P., Csányi, G. & Ceriotti, M. Comparing molecules and solids across structural and alchemical space. *Phys. Chem. Chem. Phys.* **18**, 13754–13769 (2016).

62. Van Der Maaten, L. & Hinton, G. Visualizing Data using t-SNE. *J. Mach. Learn. Res.* **9**, 2579–2605 (2008).

63. Bartók, A. P. *et al.* Machine learning unifies the modeling of materials and molecules. *Sci. Adv.* **3**, (2017).

64. De, S., Musil, F., Ingram, T., Baldauf, C. & Ceriotti, M. Mapping and classifying molecules from a high-throughput structural database. *J. Cheminform.* **9**, 1–14 (2017).

65. Dral, P. O., Quantum Chemistry in the Age of Machine Learning, Ed. Elsevier, 2023.